

Electronic supplementary information

Gas-flow activation of MOFs: unlocking efficient catalysis through dynamic bonding

Mariana L. Díaz-Ramírez,^{‡ab} Sun Ho Park,^{‡a} Marcos Rivera-Almazo,^{‡c} Erika Medel,^{‡c} Ricardo A. Peralta,^c Ilich A. Ibarra,^d Rubicelia Vargas,^{*c} Jorge Garza^{*c} and Nak Cheon Jeong^{*ab}

^aDepartment of Physics & Chemistry, DGIST, Daegu 42988, Korea

^bCenter for Basic Science, DGIST, Daegu 42988, Korea

^cDepartamento de Química, División de Ciencias Básicas e Ingeniería, Universidad Autónoma Metropolitana, Iztapalapa, CP 09340 CDMX, México

^dLaboratorio de Físicoquímica y Reactividad de Superficies (LaFREs), Instituto de Investigaciones en Materiales, Universidad Nacional Autónoma de México, Circuito Exterior s/n, CU, Del. Coyoacán, 04510, Ciudad de México, México

*To whom correspondence should be addressed. Email: ruvf@xanum.uam.mx; jgo@xanum.uam.mx; nc@dgist.ac.kr

[‡]M. L. D.-R., S. H. P., M. R.-A., and E. N.-M. contributed equally to this work.

Table of contents

Section S1. Experimental Section.....	S3
Section S2. SEM Images of HKUST-1, MOF-14, and UTSA-76 Crystals	S5
Section S3. Phase and Chemical Purities of Solvent-Loaded HKUST-1 Samples.....	S6
Section S4. In Situ Raman Spectra of Solvent-Loaded HKUST-1s under Dry N ₂ Flow	S7
Section S5. Calculation of Thermal Energy Gain	S16
Section S6. Calculation of Density Functional Theory (DFT).....	S17
Section S7. Calculation of Atoms-In-Molecules (AIM)	S20
Section S8. In Situ Raman Spectra of Solvent-Loaded HKUST-1s under Dry Ar Flow	S22
Section S9. Calculation for Kinetic Energy of Inert Gas Flow	S26
Section S10. Raman Spectra of HKUST-1 Samples Activated under N ₂ and Ar Flow Conditions.....	S28
Section S11. Quantitative Determination of Pore-Filling and Coordinating Solvents in HKUST-1 from TGA Results	S29
Section S12. Phase and Chemical Purities of Ar-Flow Activated HKUST-1 Bulk Samples	S31
Section S13. Catalytic Hydrogenation of Acetophenone.....	S33
Section S14. In-situ Raman Spectra of Ethanol-Loaded Copper-Based MOF under Static and Dry Ar Flow Conditions.....	S40
References	S40

Section S1. Experimental Section

Materials. All reagents were sourced commercially from Sigma Aldrich, Alfa Aesar, or Daejung. Copper (II) chloride dihydrate ($\text{CuCl}_2 \cdot 2\text{H}_2\text{O}$, 99%, Aldrich) and hydrochloric acid (HCl, 37%, Aldrich) were used for synthesizing large HKUST-1 crystals. Distilled deionized water (DDW), methanol (MeOH, 99.5%, Daejung), ethanol (EtOH, 94.5%, Daejung), N,N-dimethylformamide (DMF, 99.5%, Daejung), trichloromethane (CHCl_3 , TCM, 99.0%, Alfa), dichloromethane (CH_2Cl_2 , DCM, 99.5%, Daejung), dimethyl sulfoxide (DMSO, 99.5%, Sigma Aldrich), and acetonitrile (MeCN, 99.8%, Aldrich) were used for loading on HKUST-1 crystals. All solvents, except DDW, were purified using zeolite 3A in a moisture-free argon-filled glovebox to remove water prior to use as previously reported.¹

Synthesis of HKUST-1 crystals. Large HKUST-1 crystals, averaging 400 μm , were synthesized according to previously described methods.²

Loading of solvents on activated HKUST-1 crystals. A vial-in-vial technique was employed for the solvent loading. Approximately 20 mg of activated HKUST-1 crystals were placed inside a small open vial, which was then positioned in a larger vial containing 1 mL of the corresponding solvent (EtOH, MeOH, MeCN, DCM, TCM, DMF, or DMSO). The larger vial was sealed and left for 24 hours for loading EtOH, MeOH, MeCN, DCM, and TCM, and for 72 hours for loading DMF and DMSO. For water-loaded crystals, activated HKUST-1 was exposed to air for 24 hours prior to experiments. The samples were designated as EtOH-HK, MeOH-HK, MeCN-HK, DCM-HK, TCM-HK, DMF-HK, DMSO-HK, and H₂O-HK, respectively. Prior to conduct Raman studies, the structural integrity and phase purity of the solvent-loaded HK samples were verified by powder X-ray diffraction (PXRD), and chemical purity was confirmed by ¹H NMR, as detailed in Section S2, Fig. S1.

In-situ Raman spectra measurements at variable temperature. Within an Ar-charged glovebox, the HKUST-1 samples (several tens crystals) were loaded into a sealed Linkam cell equipped with CaF_2 windows. The cell was immediately removed from the glovebox, and Raman spectra were recorded using a 532-nm laser focused on a crystal through a 10X magnifying long-working-distance objective lens with an estimated spot size of about 10 μm^2 . The laser power was restricted to 1.0 mW to minimize activation, with a 6-second exposure per 30 scans. Spectra were recorded every 5 minutes for the first 30 minutes, then every 15 minutes for the duration of the experiment. Initial spectra were taken at 25 °C without nitrogen flow, followed by a variable temperature sequence with dry nitrogen or argon flow at a rate of 50 mL·min⁻¹, maintaining temperatures of 25 °C for two hours, then 40, 50, 60, and 90 °C for one hour each, followed by 45 minutes each at 120, 150, and 180 °C. The heating rate was consistently maintained at 10 °C·min⁻¹.

Thermogravimetric analyses with isothermal steps. A platinum pan was zeroed on a thermogravimetric analyzer before being transferred to the Ar-charged glovebox, where the corresponding sample was loaded. The sample-loaded pan was quickly moved from the glovebox to the analyzer in a tightly sealed vial to prevent moisture adsorption. TGA steps paralleled those of the Raman spectroscopy procedure. The heating rate for all steps was 10 °C·min⁻¹. The balance and the sample flows were 40 and 50 mL·min⁻¹, correspondingly.

Bulk Argon flow activation of solvent-exchanged HKUST-1. As-synthesized crystals were exchanged with EtOH over three days, with two solvent changes per day. Excess solvent was decanted, and the crystals were dried at room temperature under vacuum for one hour. This treatment removed excess solvent but did not yield the open state of open metal sites. Subsequently, the crystals were placed in a U-shaped drying tube with a frit to hold the sample and allow Ar to flow through. 200 mg of crystals were carefully placed in the U-shaped drying tube with the aid of a long-stem glass funnel to prevent adherence to the drying tube walls. Once uniformly spread, the crystals formed a bed approximately 4 mm in height. The cross-sectional area of the tube was approximately 1.6 cm² (1.4 cm in diameter). After sealing the joints with silicon grease, the tube was connected to an Ar line and submerged in an oil bath to maintain the activation temperature. After 24 hours of Ar flow at the set temperatures, the tube was transferred to an Ar-charged glovebox for further processing. Samples were labeled according to the activation conditions and flow rates. Further structural, textural, and chemical characterizations are detailed in Section S10, Fig. S18 and S19.

Catalytic hydrogenation reaction of acetophenone. To assess catalytic activity, we ensured no proton donors were present during reactions to avoid masking the conversion of acetophenone. Commercial Basolite C300, which exhibited superior catalytic activity compared to our in-house synthesized HKUST-1, was used. Inside an Ar-charged glovebox, HK was solvent-exchanged with MeCN over a week with daily solvent changes. After activation at 90 °C under Ar flow for 24 hours, the treated HK was used for the catalytic reaction (Ar-Act_EtOH-HK at 90 °C). Specifically, 40 mg (66 μmol) of activated HKUST-1 powders were placed in a vial containing 2 mL of dried TCM solvent. Then, 93.5 μL (1.00 mmol) of acetophenone and 295.8 μL (3.00 mmol) of phenylsilane were added to the vial, and the vial was stirred in the solvent at 25 °C for various times and analyzed by ¹H NMR to determine the conversion efficiency. Thermally activated HKUST-1 (Thermal-Act_EtOH-HK at 180 °C),

MeCN-coordinated HKUST-1 (MeCN-HK), Ar-activated MOF-14 (Ar-Act_MeCN-MOF-14), MeCN-coordinated MOF-14 (MeCN-MOF-14), Ar-activated UTSA-76 (Ar-Act_MeCN-UTSA-76), and MeCN-coordinated UTSA-76 (MeCN-UTSA-76) samples were also tested with the same amount (66 mmol) for comparison.

Theoretical calculations.

DFT calculations were performed for HKUST-1, incorporating a single molecule per unit cell (occupation ratio solvent: OMSs of 1:12) of H₂O, N₂, MeOH, EtOH, MeCN, DMF, and DCM. Higher occupation ratios for systems containing H₂O and N₂ were also explored. Full optimization procedures for the activated MOF, including both cell parameters and atomic coordinates, were carried out for the ferromagnetic state, starting from the crystallographic data. This optimized system served as the basis for including a solvent molecule. For H₂O, the crystallographic data of hydrated HKUST-1 was used as the starting point. Initial positions for each solvent molecule were proposed near the OMSs, oriented based on calculated Molecular Electrostatic Potentials (MEP).

All our calculations, including those for solvent-isolated molecules, were performed at the B3LYP-D*/POB-TZVP levels of theory^{3,4} using the Crystal14 code.⁵ Interaction energy per molecule (E_{int}) values were calculated using the equation:

$$E_{\text{int}} = (E_{\text{MOF+Sol}} - (E_{\text{MOF}} + n E_{\text{Sol}})) / n \quad (1)$$

where the subscript indicates the system for which that energy was calculated ($E_{\text{MOF+Sol}}$ for MOF with n-molecules of solvent, E_{MOF} for the pure MOF, and E_{Sol} for a single molecule), and n represents the number of molecules inside the unit cell.

With the optimized geometric systems, we further analyzed the intermolecular interactions via the Quantum Theory of Atoms In Molecules (QTAIM)⁶ and the Non-Covalent Interactions (NCI) index.⁷ We utilized a developer version of the GPUAM code for these calculations.^{8,9}

Synthesis of HKUST-1 crystals. CuCl₂·2H₂O (1.47 g, 8.6 mmol) was dissolved in 200 mL of DDW in a glass bottle. Then, 2.20 g of DMF was added to the CuCl₂ solution. In another Schott bottle, H₃BTC (2.10 g, 10 mmol) was dissolved in 200 mL of EtOH, and 0.25 g of HCl was added to the H₃BTC solution. Subsequently, the CuCl₂ solution was quickly added to the bottle containing the H₃BTC solution. After sealing the bottle with a polypropylene cap, it was placed in a preheated oven at 80 °C for 5 days. Once the product cooled to room temperature, pristine large HKUST-1 crystals were collected and washed with a 1:1 solvent mixture of DDW and EtOH.

Thermal activation of HKUST-1. Pristine HKUST-1 crystals were thermally activated to remove the coordinated and pore-filling H₂O and EtOH molecules before loading other solvents. These crystals were placed in a Schlenk tube, which was then heated to 180 °C for 16 hours under a dynamic vacuum (approximately 10⁻³ Torr). After the activation, the tube was transferred into a moisture-free, Ar-charged glovebox. The same procedure was employed to activate Basolite C300 for catalytic reactions, and this was labeled as Thermal-Act_EtOH at 180 °C.

Instrumentation. DDW was obtained from a water purification system (Merck Millipore, MQ Direct8). ¹H nuclear magnetic resonance (NMR) spectra were recorded using an AVANCE III HD FT-NMR spectrometer (Bruker, 400 MHz for ¹H). The ¹H chemical shifts were referenced to the residual proton resonance of the solvent. Raman spectra were recorded with a spectral resolution of 2 cm⁻¹ FWHM using a DXR™2xi confocal Raman imaging microscope (ThermoScientific), equipped with a high-resolution grating (1800 grooves/mm). The model of the Linkam cell used was THMS350V. Nitrogen adsorption/desorption isotherms of the samples were obtained at 77 K using a Belsorp Max surface area and porosity analyzer (BEL Japan, Inc.). Thermogravimetric analysis (TGA) was performed using Thermobalance Q50 (TA instruments). Powder X-ray diffraction (PXRD) patterns of the samples were recorded on a PANalytical diffractometer (Empyrean) with a monochromatic nickel-filtered Cu K α beam. Scanning electron microscopy (SEM) images were obtained from an FE-SEM (Hitachi S-4800) operated at an acceleration voltage of 3 kV after samples were coated by Au-Pt alloys.

Section S2. SEM Images of HKUST-1, MOF-14, and UTSA-76 Crystals

An insightful reviewer asked us to determine the average crystal sizes. To address this suggestion, we have conducted the SEM measurements. As a result, the SEM images show that the crystal sizes of HKUST-1, MOF-14, and UTSA-76 are distributed in approximately 10-20 μm .

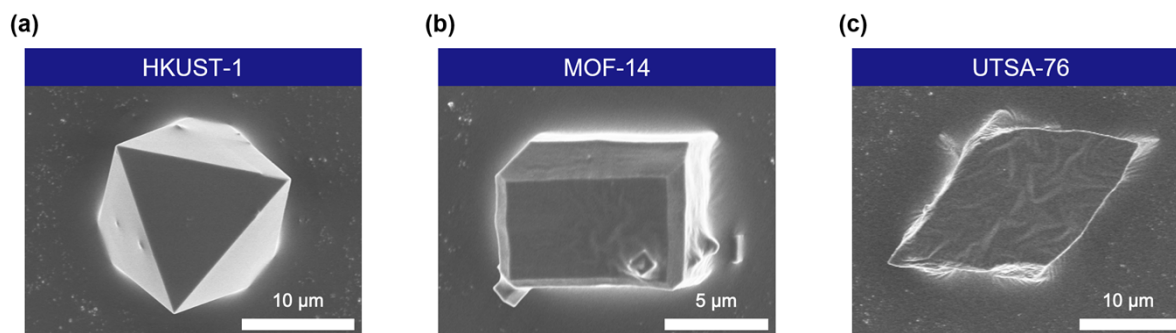


Fig. S1 SEM images of (a) HKUST-1, (b) MOF-14, and (c) UTSA-76 crystals that have approximately 10-20 μm in size.

Section S3. Phase and Chemical Purities of Solvent-Loaded HKUST-1 Samples

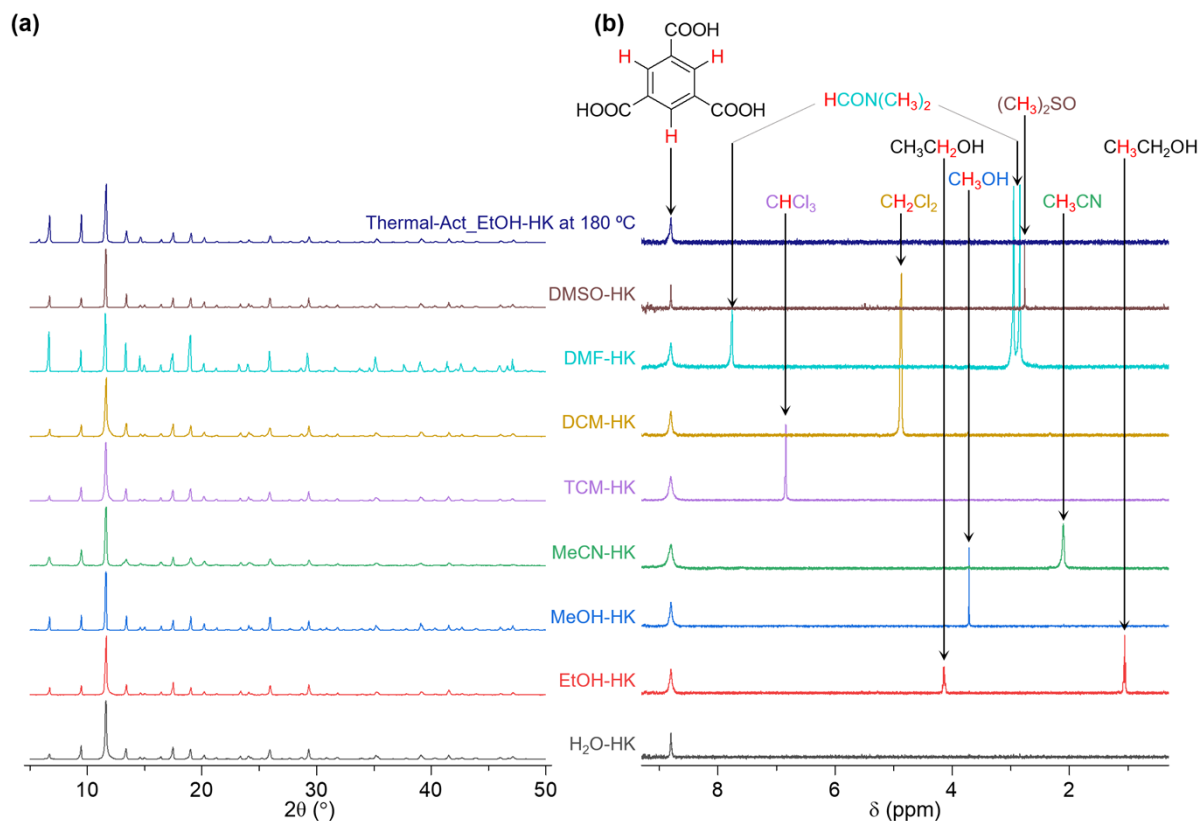


Fig. S2 (a) PXR patterns and (b) ^1H NMR spectra of DCM-, TCM-, H_2O -, MeOH-, MeCN-, EtOH-, DMF-, and DMSO-HK samples prepared for in situ Raman experiments. Thermal-Act_EtOH-HK at 180 °C was also examined for comparison. ^1H NMR spectra were recorded after the samples were entirely digested in concentrated deuterated sulfuric acid, D_2SO_4 .

Section S4. In Situ Raman Spectra of Solvent-Loaded HKUST-1s under Dry N₂ Flow

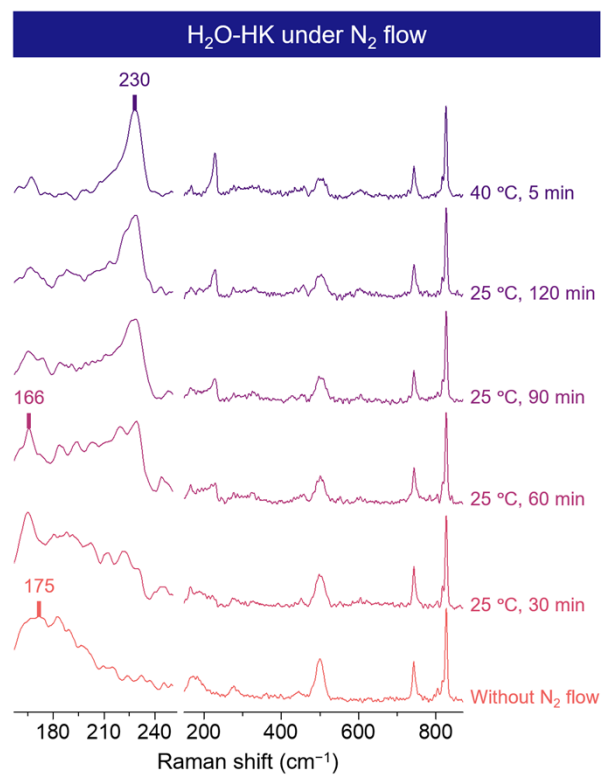


Fig. S3 Narrow (left) and wide (right) views of In situ Raman spectra of H₂O-HK sample activated under a N₂ flow of 50 mL·min⁻¹ at various temperatures and durations as indicated.

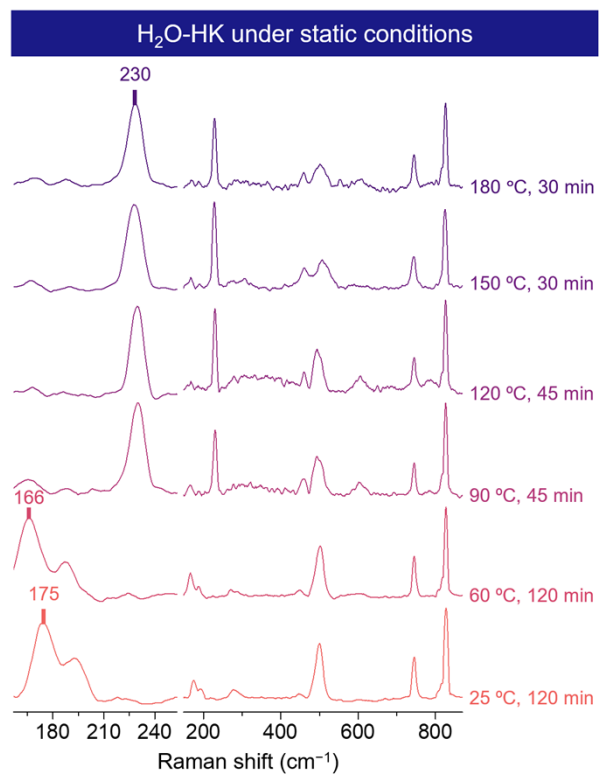


Fig. S4 Narrow (left) and wide (right) views of In situ Raman spectra of H₂O-HK sample activated under static conditions at various temperatures and durations as indicated.

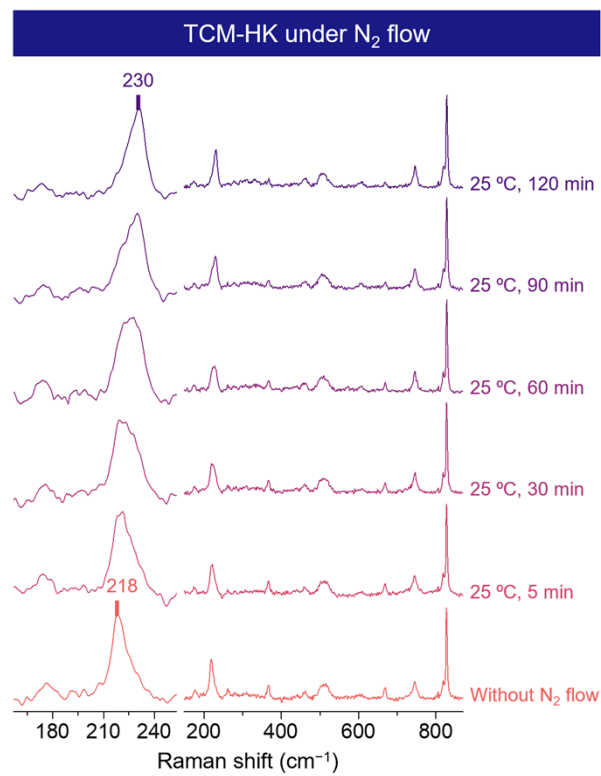


Fig. S5 Narrow (left) and wide (right) views of In situ Raman spectra of TCM-HK sample activated under a N₂ flow of 50 mL·min⁻¹ at various temperatures and durations as indicated.

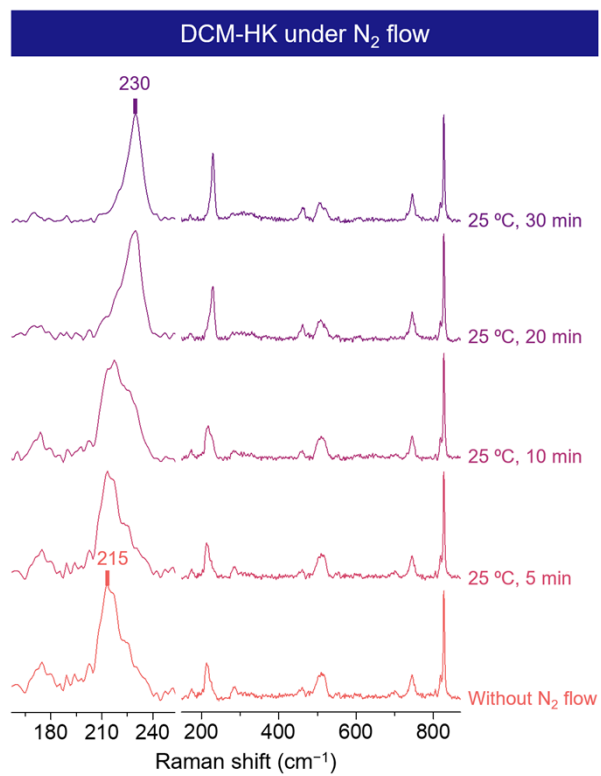


Fig. S6 Narrow (left) and wide (right) views of In situ Raman spectra of DCM-HK sample activated under a N₂ flow of 50 mL·min⁻¹ at various temperatures and durations as indicated.

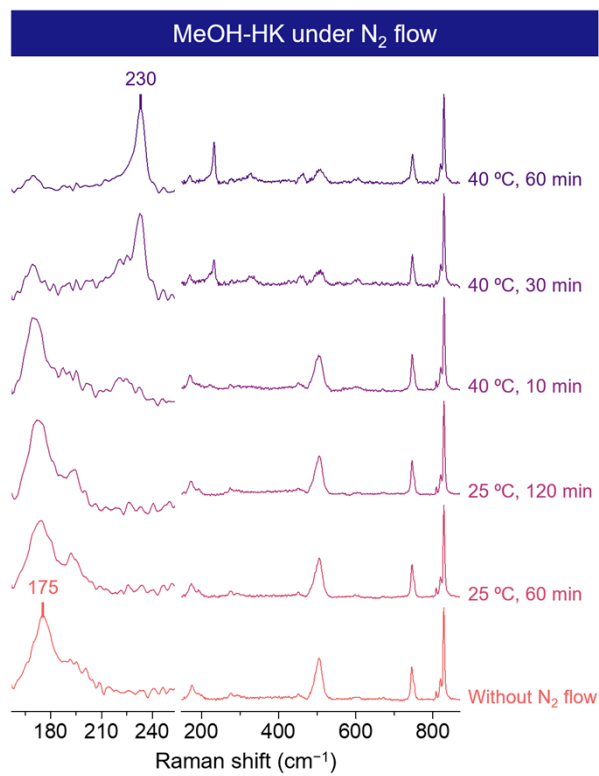


Fig. S7 Narrow (left) and wide (right) views of In situ Raman spectra of MeOH-HK sample activated under a N₂ flow of 50 mL·min⁻¹ at various temperatures and durations as indicated.

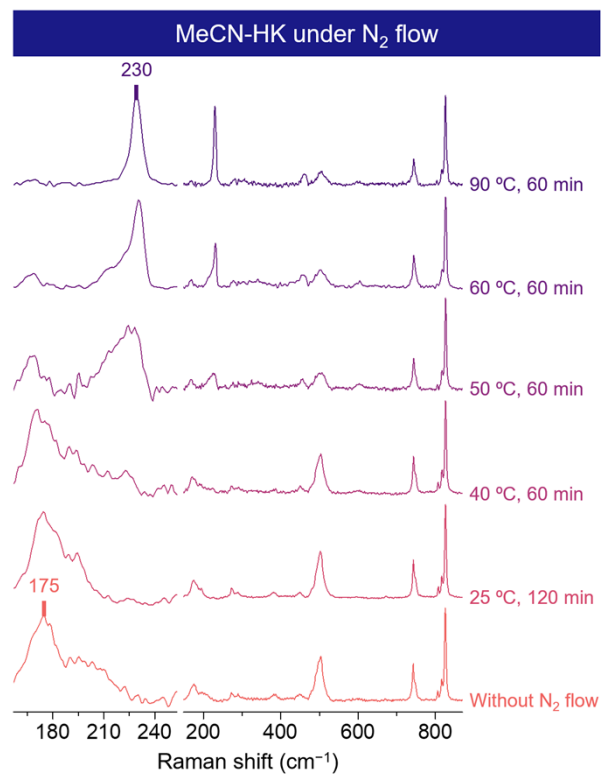


Fig. S8 Narrow (left) and wide (right) views of In situ Raman spectra of MeCN-HK sample activated under a N₂ flow of 50 mL·min⁻¹ at various temperatures and durations as indicated.

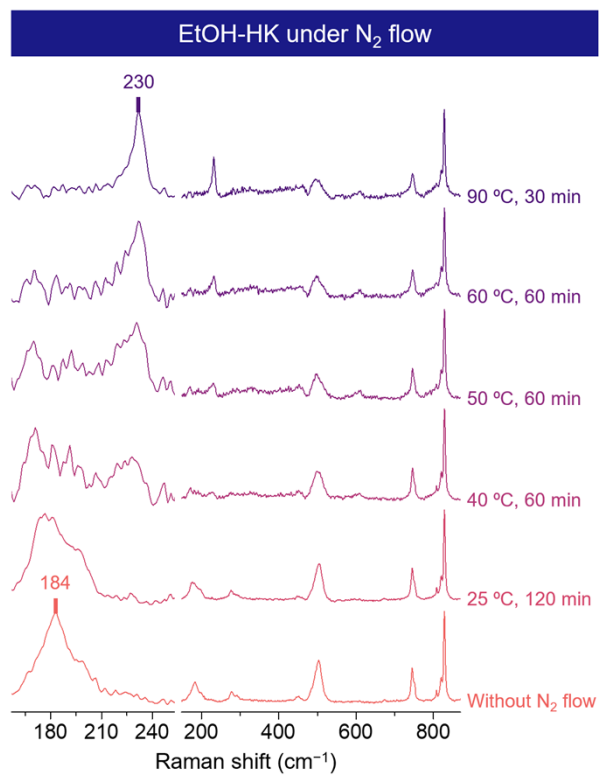


Fig. S9 Narrow (left) and wide (right) views of In situ Raman spectra of EtOH-HK sample activated under a N₂ flow of 50 mL·min⁻¹ at various temperatures and durations as indicated.

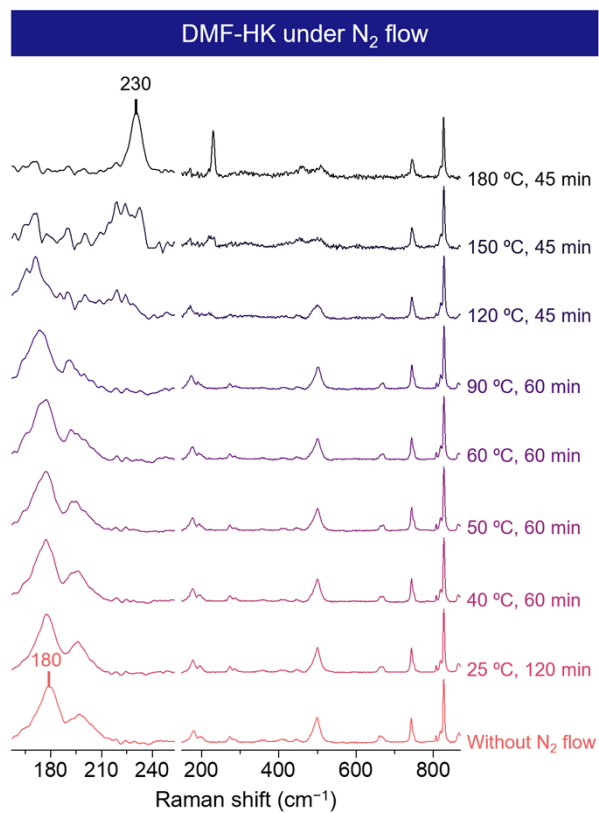


Fig. S10 Narrow (left) and wide (right) views of In situ Raman spectra of DMF-HK sample activated under a N₂ flow of 50 mL·min⁻¹ at various temperatures and durations as indicated.

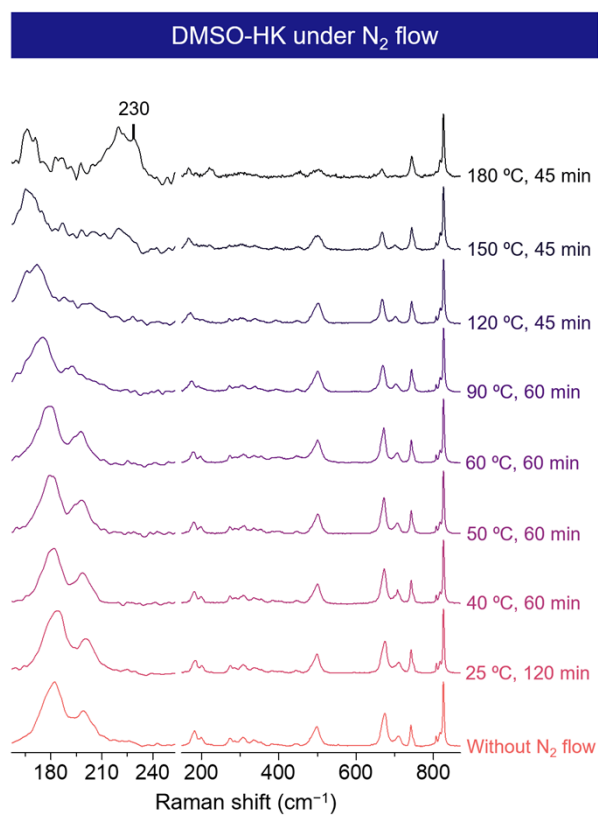


Fig. S11 Narrow (left) and wide (right) views of In situ Raman spectra of DMSO-HK sample activated under a N₂ flow of 50 mL·min⁻¹ at various temperatures and durations as indicated.

Section S5. Calculation of Thermal Energy Gain

An insightful reviewer asked us to add an energy gain of N₂-flow activation method. Therefore, we have calculated an energy gain to compare the thermal energy requirements of our gas-flow activation method with the static condition.

The thermal energy (Q) is defined as:

$$Q = C \times \Delta T \quad (1)$$

Q = Thermal energy [J g⁻¹]

m = Weight of the MOF sample (g)

C = Heat capacity of the MOF (J g⁻¹ K⁻¹)

ΔT = Temperature change (K)

The heat capacity of HKUST-1 is 0.775 J g⁻¹ K⁻¹.¹⁰

For H₂O coordinated HKUST-1 (H₂O-HK), 363 K is required for activation under static conditions, so Q_{Static} is

$$\begin{aligned} Q_{\text{Static}} &= 0.775 \text{ J g}^{-1} \text{ K}^{-1} \times (363 \text{ K} - 298 \text{ K}) \\ Q_{\text{Static}} &= 0.775 \text{ J g}^{-1} \text{ K}^{-1} \times 65 \text{ K} \\ Q_{\text{Static}} &= 50.375 \text{ J g}^{-1} \end{aligned} \quad (2)$$

For H₂O-HK, 313 K is required for activation under N₂-flow conditions, so Q_{N₂-flow} is

$$\begin{aligned} Q_{\text{N}_2\text{-flow}} &= 0.775 \text{ J g}^{-1} \text{ K}^{-1} \times (313 \text{ K} - 298 \text{ K}) \\ Q_{\text{N}_2\text{-flow}} &= 0.775 \text{ J g}^{-1} \text{ K}^{-1} \times 15 \text{ K} \\ Q_{\text{N}_2\text{-flow}} &= 11.625 \text{ J g}^{-1} \end{aligned} \quad (3)$$

Therefore, the energy gain (Q_{gain}) of the N₂-flow activation method in H₂O-HK compared to the static condition is

$$\begin{aligned} Q_{\text{gain}} &= Q_{\text{N}_2\text{-flow}} - Q_{\text{Static}} \\ &= 11.625 \text{ J g}^{-1} - 50.375 \text{ J g}^{-1} \\ &= -38.750 \text{ J g}^{-1} \end{aligned}$$

Therefore, the N₂-flow activation method has an energy gain of 38.750 J g⁻¹ compared to the static condition.

Section S6. Calculation of Density Functional Theory (DFT)

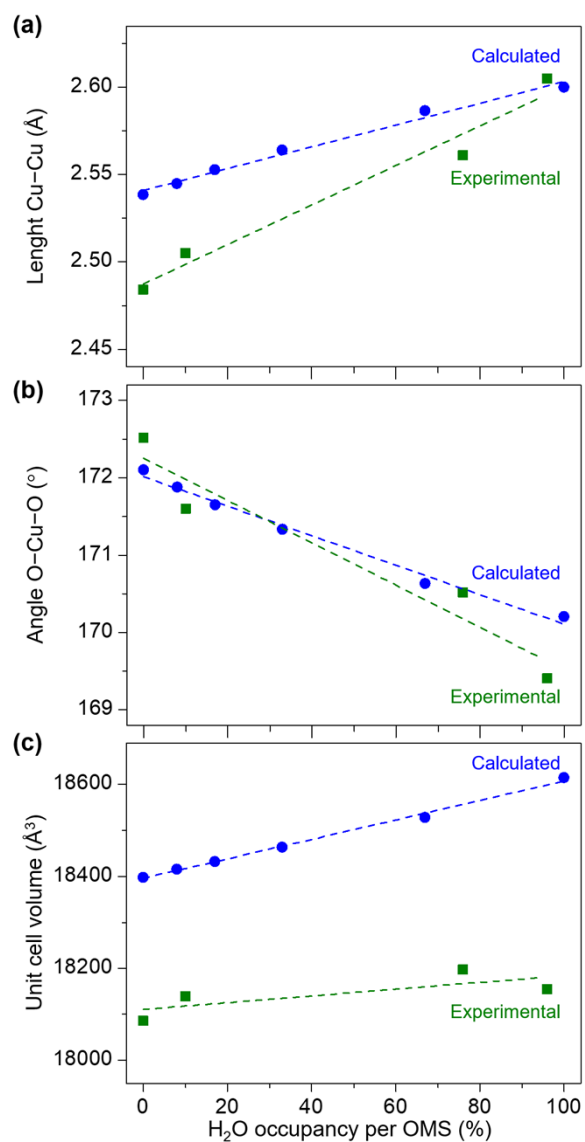


Fig. S12 Comparative analysis of experimental (green) and DFT-calculated (blue) data showing changes in (a) Cu-Cu bond length, (b) O-Cu-O bond angle, and (c) unit cell volume as a function of H₂O occupancy percentage at OMS sites.

The selected method, previously reported for studying HKUST-1,^{11, 12} returned acceptable optimized geometry parameters, with deviations of 1.7% in volume and 2.2% in Cu–Cu distance, both relative to experimental data. These geometrical changes are compatible with the volume expansion observed experimentally when the temperature is decreased, corroborated by crystallographic data.

Starting from the DFT-optimized geometry, we included varying amounts of water molecules per unit cell, occupying 1, 2, 4, 8, and 12 Cu-sites per unit cell, which corresponded to 8%, 17%, 33%, 67%, and 100% of the available OMSs, respectively. Except for the 8% case, the molecules were included in symmetrically selected Cu paddlewheel pairs. The parameters that exhibited a linear correlation with the number of adsorbed water molecules were the Cu–Cu length, O–Cu–O angle, and unit cell volume, as displayed in Tables S1-3 and Fig. S11. Notably, the relationship between Cu–Cu length and water content is reflected in the change of the vibrational frequency of the Cu–Cu pair. Specifically, when the Cu centers are in an open state, i.e., without coordinated water molecules, the metal centers are closer together, as both theoretical and experimental results have shown. Consequently, a higher vibrational frequency can be expected, and indeed, it is measured in Raman spectroscopy ($\nu = 230 \text{ cm}^{-1}$). As water molecules begin to occupy Cu sites, and partial electron donation from coordinating water molecules to the antibonding molecular orbital of the Cu^{2+} ion occurs, the bond between Cu centers loosens, resulting in a decrease in vibrational frequency to $\nu = 166 \text{ cm}^{-1}$ when only Cu-coordinated water molecules are present. This was demonstrated previously in a report on the crystalline arrangement of water molecules inside HKUST-1.¹³ Moreover, contrasting our theoretical results, we generally found good agreement with the observed experimental linear behavior, further validating the selected computational method and supporting the observations previously reported.

Table S1. Comparison of Experimental and Calculated Cu–Cu Bond Lengths at Various H₂O Occupancies in HKUST-1

Experimental		Calculated	
H ₂ O occupancy for OMS (%)	Length Cu–Cu (Å)	H ₂ O occupancy for OMS (%)	Length Cu–Cu (Å)
0	2.48	0	2.54
10	2.51	8	2.54
76	2.56	17	2.55
100	2.62	33	2.56
		67	2.59
		100	2.60

Table S2. Comparison of Experimental and Calculated $\angle\text{O–Cu–O}$ Bond Angle at Various H₂O Occupancies in HKUST-1

Experimental		Calculated	
H ₂ O occupancy for OMS (%)	$\angle\text{O–Cu–O}$ (°)	H ₂ O occupancy for OMS (%)	$\angle\text{O–Cu–O}$ (°)
0	172.52	0	172.10
10	171.60	8	171.88
76	170.51	17	171.65
100	168.78	33	171.33
		67	170.63
		100	170.20

Table S3. Comparison of Experimental and Calculated Unit Cell Volume at Various H₂O Occupancies in HKUST-1

Experimental		Calculated	
H ₂ O occupancy for OMS (%)	V (Å ³)	H ₂ O occupancy for OMS (%)	V (Å ³)
0	18086	0	18398
10	18139	8	18416
76	18197	17	18432
100	18184	33	18464
		67	18528
		100	18615

To explain the observed dissociation temperatures of each coordinated solvent, we estimated the interaction energy per molecule (E_{int}) using models with a single solvent molecule per unit cell for the following solvents: DCM, N_2 , H_2O , MeOH, MeCN, EtOH, and DMF (Section S4, Table S4). Generally, there is agreement between the increasing order of E_{int} at different solvent-coordinated Cu centers and the corresponding experimentally measured dissociation temperatures. However, MeOH and MeCN exhibit an inverse order between calculated E_{int} and experimental activation temperatures, which can be attributed to the inherent differences between our approximation and the experimental conditions. While our approximation considered only one solvent molecule in the unit cell, during the experiments, other molecules were also present in the pores as pore-filling solvents, leading to additional interactions between Cu-coordinated and pore-filling solvent molecules, which affected the overall E_{int} .

Table S4. Geometric Parameters and Interaction Energies of Various Solvents-Coordinated Cu Centers in HKUST-1

Solvent	Cu...Solvent (Å)	Cu...Cu (Å)	$\angle\text{O-Cu-O}$ (°)	E_{int} (kcal/mol)
DCM I	2.83	2.58	166.6 / 170.2	-1.2
DCM II	2.69	2.58	167.9 / 169.2	-1.2
N_2	2.32	2.56	180.0 / 180.0	-6.5
H_2O	2.21	2.59	167.0 / 167.0	-12.5
MeOH	2.20	2.60	163.9 / 169.9	-16.9
MeCN	2.14	2.63	164.4 / 163.6	-16.4
EtOH	2.19	2.60	163.7 / 168.8	-17.9
DMF	2.10	2.62	166.2 / 166.1	-18.5

Table S5. Geometric Parameters and Interaction Energies of H_2O -, MeOH-, and MeCN-Coordinated Cu Centers in HKUST-1

Solvent	Cu...Solvent (Å)	Cu...Cu (Å)	E_{int} (kcal/mol)
$\text{H}_2\text{O-Cu-Cu}$	2.21	2.59	-12.5
$\text{H}_2\text{O-Cu-Cu-H}_2\text{O}$	2.23	2.65	-11.9
MeOH-Cu-Cu	2.20	2.60	-16.9
MeOH-Cu-Cu-MeOH	2.21	2.65	-16.4
MeCN-Cu-Cu	2.14	2.63	-16.4
MeCN-Cu-Cu-MeCN	2.18	2.72	-14.6

Section S7. Calculation of Atoms-In-Molecules (AIM)

According to our Atoms in Molecules (AIM) analysis, the highest electron density at the bond critical point (ρ_{BCP}) was observed for MeCN, indicating the strongest interaction between Cu and the evaluated solvents. However, it is important to note that interactions between coordinated solvent molecules and pore-filling solvent molecules can affect interaction energies, which may explain the inverted order observed in our results.¹⁴ Additionally, the presence of non-conventional hydrogen bonds between the coordinated solvent molecules and the framework may account for why EtOH and DMF are strong coordinating solvents. Although MeCN displayed the highest (ρ_{BCP}) value in the solvent \cdots Cu interaction, both EtOH and DMF showed higher calculated E_{int} values than MeCN (Section S4, Table S6 and S8). Notably, MeCN formed only one solvent \cdots Cu interaction with the framework (Section S4, Tables S8-10).¹⁵ Nevertheless, the experimental trend for the dissociation temperatures of different solvents correlated well with the theoretically estimated MOF-Solvent interaction energies, affirming the predominance of the Cu-Solvent interaction in all cases but highlighting that other relevant interactions are also involved.

Table S6. Electronic Density (ρ_{BCP}), Total Density Energy (H_{BCP}), and Bond Order (H_{BCP}/ρ_{BCP}) Values at Bond Critical Points for Cu-Solvent Interactions in HKUST-1

Solvent	H_{BCP}/ρ_{BCP}	H_{BCP}	ρ_{BCP}
DCM (Mode I)	-13.831×10^{-3}	-0.316×10^{-3}	22.903×10^{-3}
DCM (Mode II)	-63.319×10^{-3}	-1.915×10^{-3}	30.252×10^{-3}
N ₂	-30.639×10^{-3}	-1.176×10^{-3}	38.397×10^{-3}
H ₂ O	-57.430×10^{-3}	-2.653×10^{-3}	46.191×10^{-3}
MeOH	-10.171×10^{-3}	-0.521×10^{-3}	51.224×10^{-3}
MeCN	-56.294×10^{-3}	-3.375×10^{-3}	59.953×10^{-3}
EtOH	-22.655×10^{-3}	-1.182×10^{-3}	52.174×10^{-3}
DMF	50.052×10^{-3}	2.808×10^{-3}	56.102×10^{-3}

Table S7. Electronic Density (ρ_{BCP}) and Its Proportion ($\% \rho_{BCP}$) Values at Bond Critical Points for Cu-MeOH Interactions and Non-Conventional Hydrogen Bond (NC-HB) in HKUST-1

Interaction of MeOH	ρ_{BCP}	$\% \rho_{BCP}$
Cu \cdots O _(MeOH)	51.224×10^{-3}	82.03
C-H _(BTC) \cdots O _(MeOH) (NC-HB)	5.187×10^{-3}	8.31
C-H _(BTC) \cdots O _(MeOH) (NC-HB)	6.032×10^{-3}	9.66

Table S8. Electronic Density (ρ_{BCP}) and Its Proportion ($\% \rho_{BCP}$) Values at Bond Critical Points for Cu-MeCN Interactions in HKUST-1

Interaction of MeCN	ρ_{BCP}	$\% \rho_{BCP}$
Cu \cdots N	59.953×10^{-3}	100.00

Table S9. Electronic Density (ρ_{BCP}) and Its Proportion ($\% \rho_{BCP}$) Values at Bond Critical Points for Cu-DMF Interactions and Non-Conventional Hydrogen Bond (NC-HB) in HKUST-1

Interaction of DMF	ρ_{BCP}	$\% \rho_{BCP}$
Cu \cdots O _(DMF)	56.102×10^{-3}	98.59
C-H _(BTC) \cdots O _(DMF) (NC-HB)	0.199×10^{-3}	0.35
C-H _(BTC) \cdots O _(DMF) (NC-HB)	0.438×10^{-3}	0.77
C-H _(BTC) \cdots O _(DMF) (NC-HB)	0.165×10^{-3}	0.29

Table S10. Electronic Density (ρ_{BCP}) and Its Proportion ($\% \rho_{BCP}$) Values at Bond Critical Points for Cu-EtOH Interactions and Non-Conventional Hydrogen Bond (NC-HB) in HKUST-1

Interaction of EtOH	ρ_{BCP}	$\% \rho_{BCP}$
Cu \cdots O _(EtOH)	52.174×10^{-3}	81.54
C-H _(BTC) \cdots O _(EtOH) (NC-HB)	6.620×10^{-3}	10.35
C-H _(BTC) \cdots O _(EtOH) (NC-HB)	5.192×10^{-3}	8.11

Table S11. Electronic Density (ρ_{BCP}) and Its Proportion ($\% \rho_{BCP}$) Values at Bond Critical Points for Cu-DCM(I) Interactions and Non-Conventional Hydrogen Bond (NC-HB) in HKUST-1

Interaction of DCM (Mode I)	ρ_{BCP}	$\% \rho_{BCP}$
Cu \cdots Cl _{1(DCM)}	22.904×10^{-3}	32.57
C-O _(BTC) \cdots H _{1(DCM)} (NC-HB)	12.751×10^{-3}	18.13
C-O _(BTC) \cdots H _{1(DCM)} (NC-HB)	7.677×10^{-3}	10.92
C-O _(BTC) \cdots Cl _{2(DCM)} (NC-HB)	5.351×10^{-3}	7.61
C-H _(BTC) \cdots Cl _{2(DCM)} (NC-HB)	5.140×10^{-3}	7.31
C-H _(BTC) \cdots H _{1(DCM)} (NC-HB)	5.017×10^{-3}	7.14
C-O _(BTC) \cdots Cl _{2(DCM)} (NC-HB)	4.985×10^{-3}	7.09
C-H _(BTC) \cdots Cl _{2(DCM)} (NC-HB)	3.796×10^{-3}	5.40
C-H _(BTC) \cdots H _{2(DCM)} (NC-HB)	2.693×10^{-3}	3.83

Table S12. Electronic Density (ρ_{BCP}) and Its Proportion ($\% \rho_{BCP}$) Values at Bond Critical Points for Cu-DCM(II) Interactions and Non-Conventional Hydrogen Bond (NC-HB) in HKUST-1

Interaction of DCM (Mode II)	ρ_{BCP}	$\% \rho_{BCP}$
Cu \cdots Cl _{1(DCM)}	30.253×10^{-3}	58.50
C-O _{1(BTC)} \cdots (C)H _{1(DCM)} (NC-HB)	5.963×10^{-3}	11.53
C-O _{2(BTC)} \cdots H _{1(DCM)} (NC-HB)	13.996×10^{-3}	27.06
C-O _(BTC) \cdots Cl _{2(DCM)} (NC-HB)	1.503×10^{-3}	2.91

Table S13. Electronic Density (ρ_{BCP}) and Its Proportion ($\% \rho_{BCP}$) Values at Bond Critical Points for Cu-N₂ Interactions in HKUST-1

Interaction of N ₂	ρ_{BCP}	$\% \rho_{BCP}$
Cu \cdots N	38.398×10^{-3}	100.00

Section S8. In Situ Raman Spectra of Solvent-Loaded HKUST-1s under Dry Ar Flow

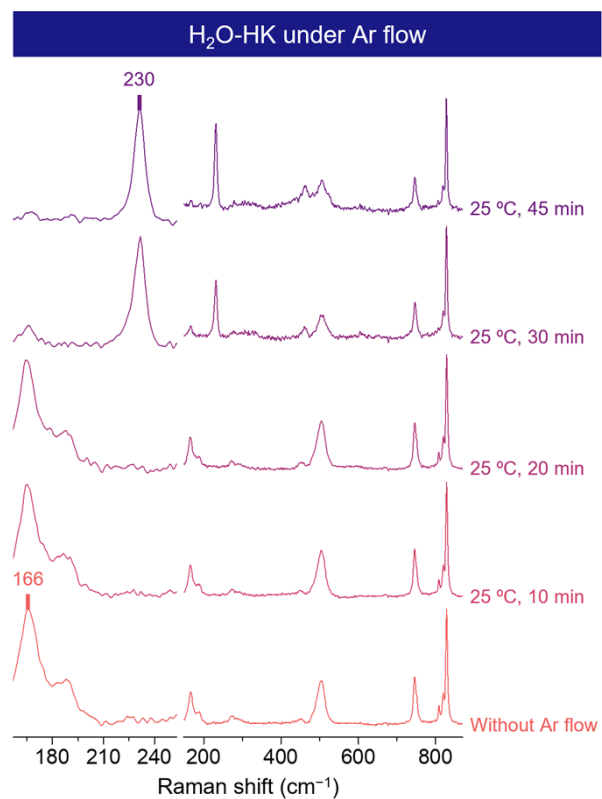


Fig. S13 Narrow (left) and wide (right) views of In situ Raman spectra of H₂O-HK sample activated under an Ar flow of 50 mL·min⁻¹ at 25 °C and various durations as indicated.

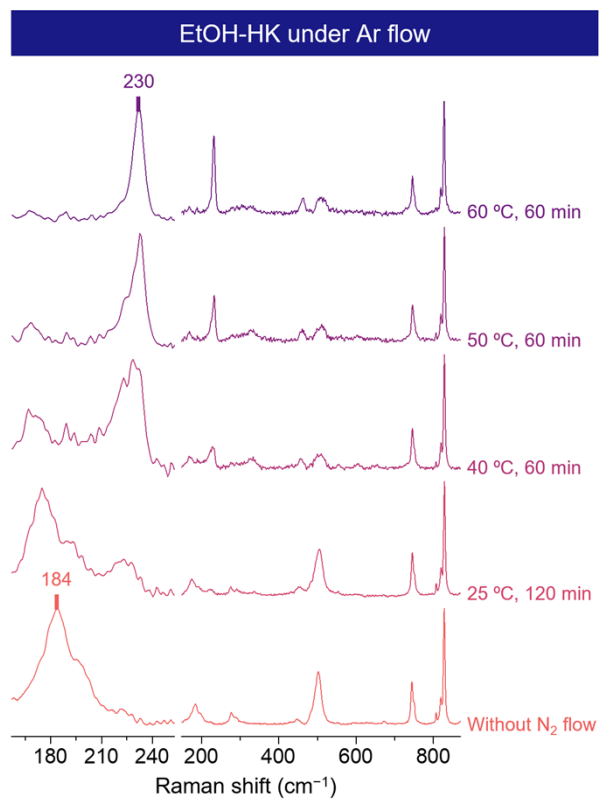


Fig. S14 Narrow (left) and wide (right) views of In situ Raman spectra of EtOH-HK sample activated under an Ar flow of $50 \text{ mL}\cdot\text{min}^{-1}$ at various temperatures and durations as indicated.

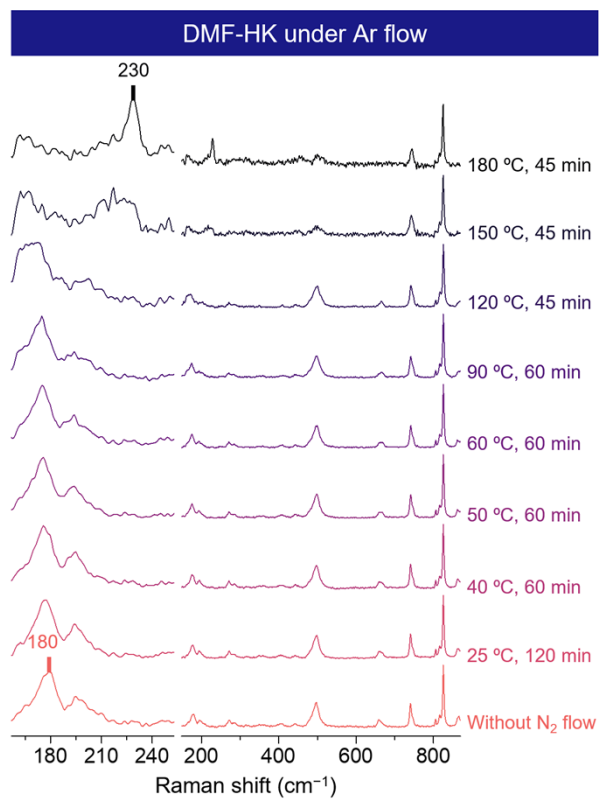


Fig. S15 Narrow (left) and wide (right) views of In situ Raman spectra of DMF-HK sample activated under an Ar flow of 50 mL·min⁻¹ at various temperatures and durations as indicated.

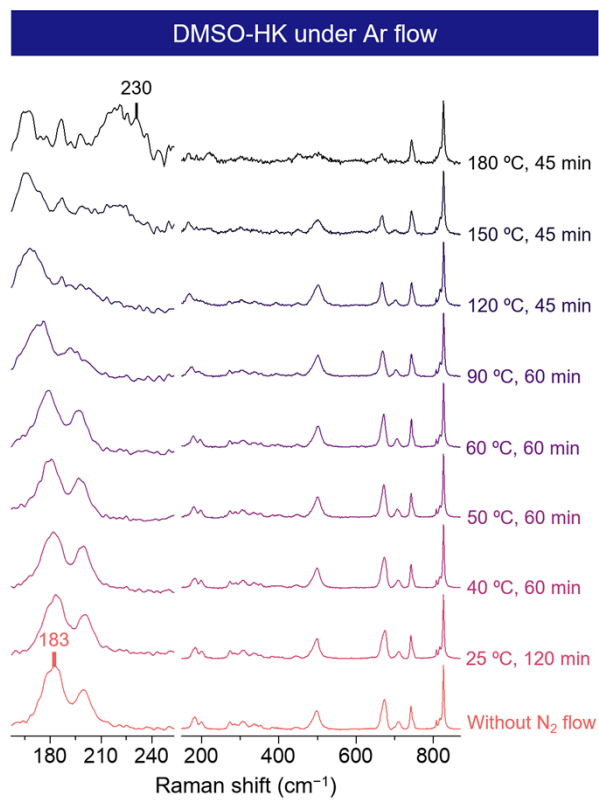


Fig. S16 Narrow (left) and wide (right) views of In situ Raman spectra of DMSO-HK sample activated under an Ar flow of $50 \text{ mL}\cdot\text{min}^{-1}$ at various temperatures and durations as indicated.

Section S9. Calculation for Kinetic Energy of Inert Gas Flow

Assuming ideal gas behavior, the kinetic energy (KE) of a flow is defined as:

$$KE = (V \cdot A \cdot \rho) \cdot \left(\frac{\alpha V^2}{2} \right) \quad (1)$$

V = average velocity of fluid [m/s]

α = kinetic energy correction factor, 2.0 for laminar flow or 1 for turbulent flow

A = Cross sectional flow area of pipe [m²]

ρ = gas density [kg/m³]

We used temperature and absolute pressure to calculate gas density, ρ .

$$\rho = \frac{m}{v} = \frac{P \cdot M}{R \cdot T}$$

$$\rho = \frac{121.985 \text{ kPa} \cdot 39.948 \text{ g/mol}}{8.314462 \frac{\text{J}}{\text{mol} \cdot \text{K}} \cdot 298 \text{ K}}$$

$$\rho = 1.96 \text{ kg/m}^3 \quad (2)$$

P = Pressure [Pa], Absolute pressure = Gauge + atmospheric pressure = 121.985 kPa

M = Molecular weight of gas [g/mol], $M_{Ar} = 39.948 \text{ g/mol}$

R = Ideal gas constant [J/mol·K] = 8.314462 J/mol·K

T = Temperature [K] = 298 K

We calculated the mass flow rate with the experimental volumetric flow rate ($Q = 50 \text{ mL/min} = 8.3 \times 10^{-7} \text{ m}^3 \cdot \text{s}^{-1}$) and density.

$$\dot{m} = Q \cdot \rho$$

$$\dot{m} = 8.3 \times 10^{-7} \frac{\text{m}^3}{\text{s}} \cdot 1.96 \frac{\text{kg}}{\text{m}^3}$$

$$\dot{m} = 1.64 \times 10^{-6} \text{ kg/s} \quad (3)$$

\dot{m} = mass flow rate [kg/s]

Q = Volumetric flow rate [m³/s].

ρ = density [kg/m³]

Next, we calculated the average velocity as follows:

$$\bar{V} = \frac{\dot{m}}{A \cdot \rho}$$

$$\bar{V} = \frac{1.64 \times 10^{-6} \frac{kg}{s}}{1.61 \times 10^{-4} m^2 \cdot 1.96 \frac{kg}{m^3}}$$

$$\bar{V} = 0.0052 \text{ m/s} \quad (4)$$

\bar{V} = Average velocity [m/s]

\dot{m} = mass flow rate [kg/s]

A = Cross-sectional area of tubing [m²].

ρ = 1.61 × 10⁻⁴ m²

Then, we could estimate the kinetic energy, KE using Eq. (1) and (4)

$$KE = (V \cdot A \cdot \rho) \cdot \left(\frac{\alpha V^2}{2} \right)$$

$$KE = (\dot{m}) \cdot \left(\frac{\alpha V^2}{2} \right)$$

$$KE = 1.64 \times 10^{-6} \frac{kg}{s} \cdot \left(\frac{2 \cdot (0.0052 \frac{m}{s})^2}{2} \right)$$

$$KE = 4.41 \times 10^{-11} \text{ J/s}$$

\bar{V} = Average velocity [m/s]

A = Cross sectional flow area of pipe [m²]

ρ = gas density [kg/m³]

\dot{m} = mass flow rate [kg/s]

α = kinetic energy correction factor, 2.0 for laminar flow or 1 for turbulent flow.

Re number was lower than 4,000 under the experimental conditions tested, so $\alpha = 2$

Section S10. Raman Spectra of HKUST-1 Samples Activated under N₂ and Ar Flow Conditions

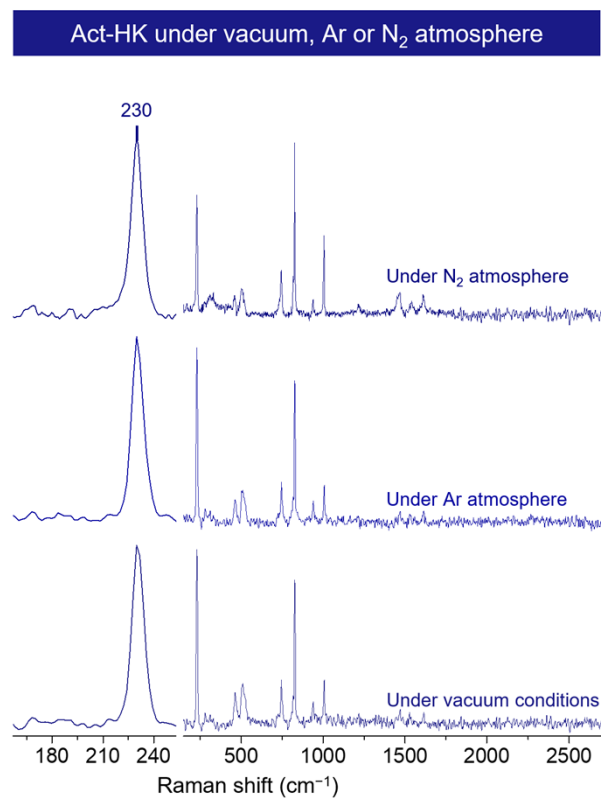


Fig. S17 Narrow (left) and wide (right) views of Raman spectra of HKUST-1 samples activated under N₂-flow, Ar-flow, and vacuum conditions as indicated.

Section S11. Quantitative Determination of Pore-Filling and Coordinating Solvents in HKUST-1 from TGA Results

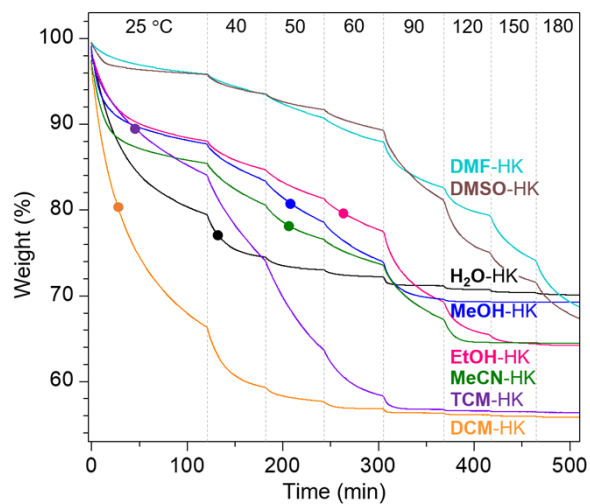


Fig. S18 Thermogravimetric analysis (TGA) profiles showing the weight loss of HKUST-1 coordinated with various solvents over time at different temperatures. The solvents include DMF (cyan), DMSO (brown), H₂O (black), MeOH (blue), EtOH (pink), MeCN (green), TCM (purple), and DCM (orange). Asterisks mark the time when each coordinated solvent begins to dissociate. The dissociation time was calculated based on the stoichiometry of 1-to-1 for the Cu-to-solvent coordination.

Table S14. Quantitative Calculation of Only Cu-coordinating H₂O in HKUST-1, Based on TGA Result

Term	Calculation	Result
(1) mass of activated HK (mg)	Final mass of TGA	6.911
(2) formula mass of Cu ₃ BTC ₂ unit (mg·mmol ⁻¹)		604.9
(3) number of Cu per Cu ₃ BTC ₂ unit		3
(4) number of Cu centers in (1) (mmol)	(1)·[(3)/(2)] = 6.911 mg·(3/604.9 mg·mmol ⁻¹)	0.034
(5) molar mass of H ₂ O (mg·mmol ⁻¹)		18.01
(6) weight of only Cu-coordinated H ₂ O (mg)	(4)·(5) = 0.034 mmol·(18.01mg·mmol ⁻¹)	0.617
(7) weight of coordinated H ₂ O and Act-HK (mg)	(1)+(6) = 6.911 mg+ 0.617 mg	7.529
(8) total initial mass (mg)	Initial mass of TGA	9.859
(9) corresponding wt% of (7) (%)	[(7)/(8)] x100 = (7.528 mg/9.859 mg) x 100	76.36

Then, 76.36 wt% is marked with an asterisk in Fig. 5 in the main text. The same calculations were followed for MeOH-, EtOH-, TCM-, DCM- and MeCN-HK samples, with their corresponding values. Furthermore, as DMF- and DMSO-HK samples did not reach a stable weight, i.e. some solvent was still adsorbed in the material by the end of the measurement, it was not possible to calculate the ratio of pore-filling and coordination solvent.

Table S15. Quantitative Calculation of Pore-Filling and Coordinating Solvents in Various HKUST-1 Samples

Sample	Asterisks mark (wt %)	Final weight (wt %)	Pore-filling solvent		Coordinating solvent	
			(wt %) ^a	(mole ratio) ^b	(wt %) ^c	(mole ratio) ^d
H ₂ O-HK	76.36	70.10	23.64	3.774	6.26	1.000
MeOH-HK	80.27	69.26	19.73	1.793	11.01	1.000
EtOH-HK	78.94	64.26	21.06	1.434	14.68	1.000
TCM-HK	89.79	56.39	10.21	0.306	33.40	1.000
DCM-HK	79.33	55.82	20.67	0.879	23.51	1.000
MeCN-HK	77.62	64.49	22.38	1.704	13.13	1.000

^a100 – Mark (wt %)

^bmole ratio of Cu to pore-filling solvent,

(pore-filling solvent/molar mass of solvent)/3*(Final weight/formula mass of Cu₃BTC₂)

^cMark (wt %) – Final weight (wt %)

^dmole ratio of Cu to coordinating solvent,

(coordinating solvent/molar mass of solvent)/3*(Final weight/formula mass of Cu₃BTC₂)

Section S12. Phase and Chemical Purities of Ar-Flow Activated HKUST-1 Bulk Samples

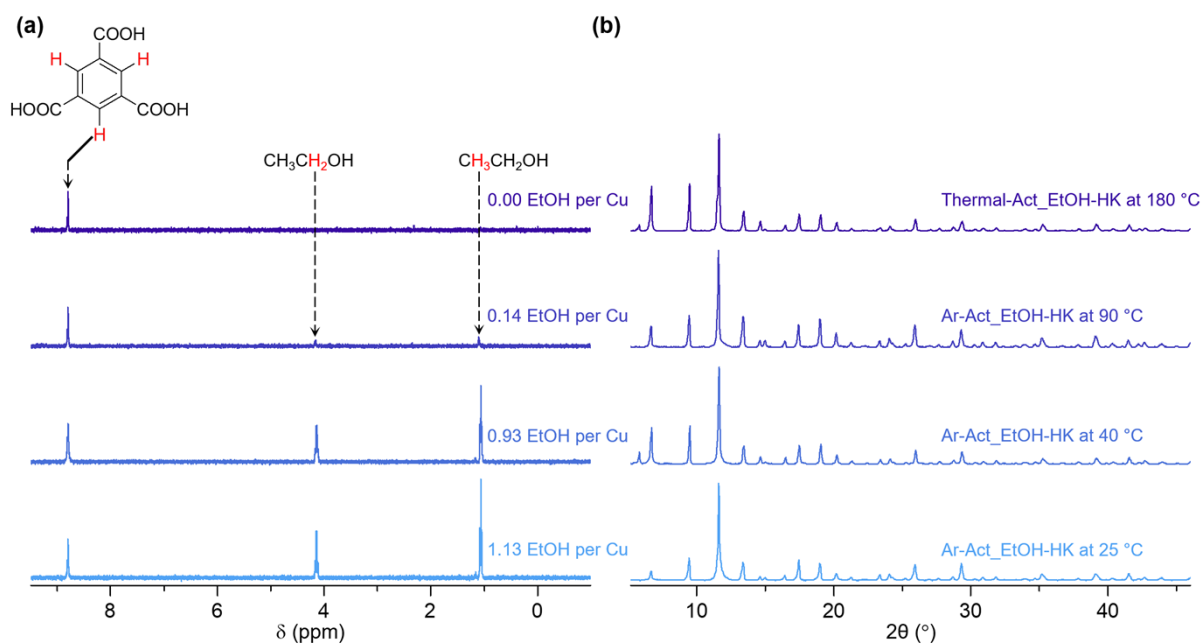


Fig. S19 (a) ^1H NMR spectra and (b) PXRD patterns of Ar-Act_EtOH-HK at 90 $^\circ\text{C}$, Ar-Act_EtOH-HK at 40 $^\circ\text{C}$, and Ar-Act_EtOH-HK at 25 $^\circ\text{C}$ samples activated under an Ar flow of $50\text{ mL}\cdot\text{min}^{-1}$. The sample of Thermal-Act_EtOH at 180 $^\circ\text{C}$ was also examined for comparison. ^1H NMR spectra were recorded after the samples were entirely digested in concentrated deuterated sulfuric acid, D_2SO_4 .

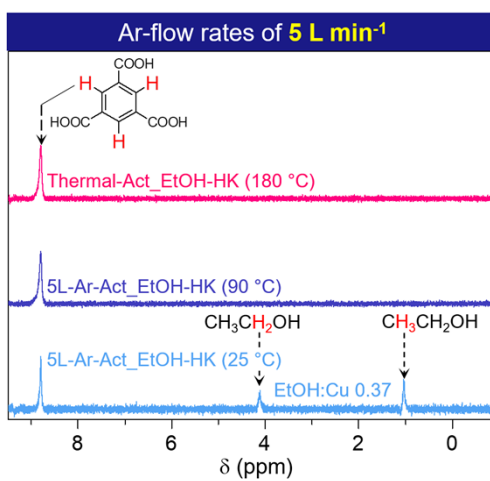


Fig. S20 ^1H NMR spectra of Ar-Act_EtOH-HK at 90 °C and Ar-Act_EtOH-HK at 25 °C samples activated under an Ar flow of 5 L·min⁻¹. The sample of Thermal-Act_EtOH at 180 °C was also examined for comparison. ^1H NMR spectra were recorded after the samples were entirely digested in concentrated deuterated sulfuric acid, D_2SO_4 .

Section S13. Catalytic Hydrogenation of Acetophenone

An insightful reviewer asked us to add a PXRD analysis of HKUST-1 after a catalytic hydrogenation reaction. In response, we performed a PXRD analysis of HKUST-1 after the catalytic reaction. The results showed that the structure of HKUST-1 collapsed completely after the catalytic reaction. We found that this observation is in good agreement with previous reports, where the HKUST-1 structure decomposes after hydrogenation catalytic reactions, thus giving rise to a limitation in recycling the catalyst.¹⁶ Our purpose of the catalytic reaction was to demonstrate how the Ar-flow activation method effectively generates metal sites in an open state and thereby enhances the catalytic activity under milder conditions. Despite the structural collapse of HKUST-1 after the reaction, the significant improvement in catalytic performance highlights the efficacy of our activation method.

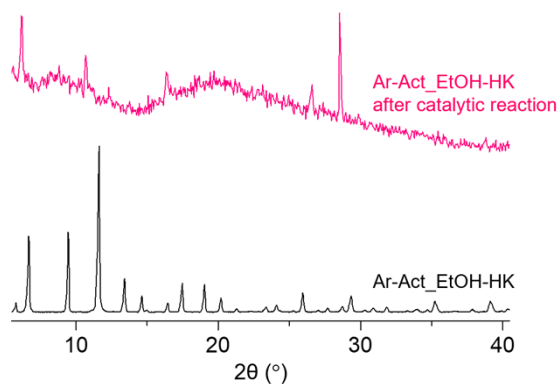


Fig. S21 PXRD patterns of Ar-Act_EtOH-HK before and after the catalytic hydrogenation reaction.

An insightful reviewer suggested to add catalytic efficiencies of Ar-activated and non-activated MeCN-MOF-14 and MeCN-UTSA-76. The results showed that Ar-Act_MeCN-MOF-14 exhibits higher catalytic activity compared to non-activated MeCN-MOF-14, demonstrating that Ar-flow activation is also effective in enhancing the catalytic performance of MOF-14. However, MeCN-UTSA-76 was challenging due to its intrinsic low catalytic efficiency of UTSA-76.

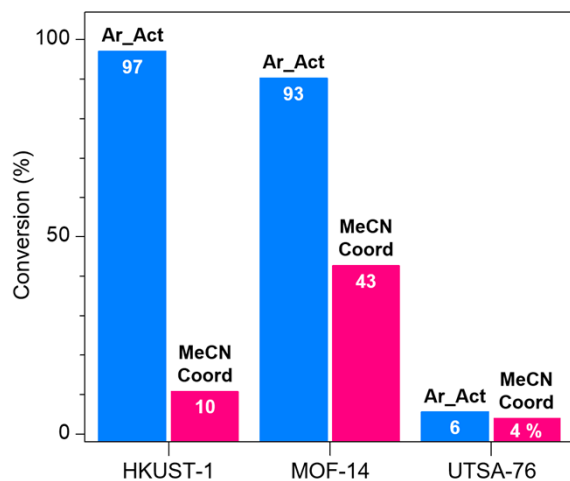


Fig. S22 Conversion efficiencies of catalytic hydrogenation reaction of Ar-activated and non-activated MeCN-HKUST-1, MeCN-MOF-14, and MeCN-UTSA-76.

Section S14. In-situ Raman Spectra of Ethanol-Loaded Copper-Based MOF under Static and Dry Ar Flow Conditions

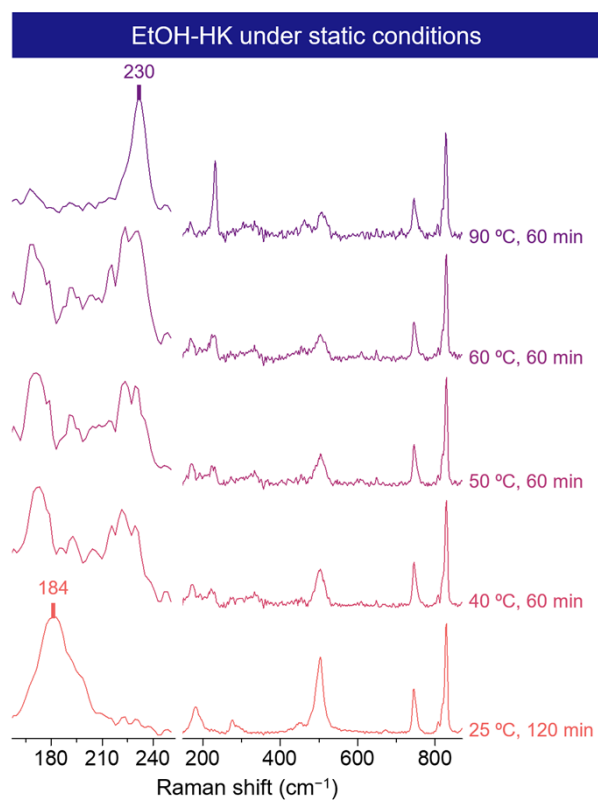


Fig. S23 Narrow (left) and wide (right) views of In situ Raman spectra of EtOH-HK sample activated under static conditions at various temperatures as indicated.

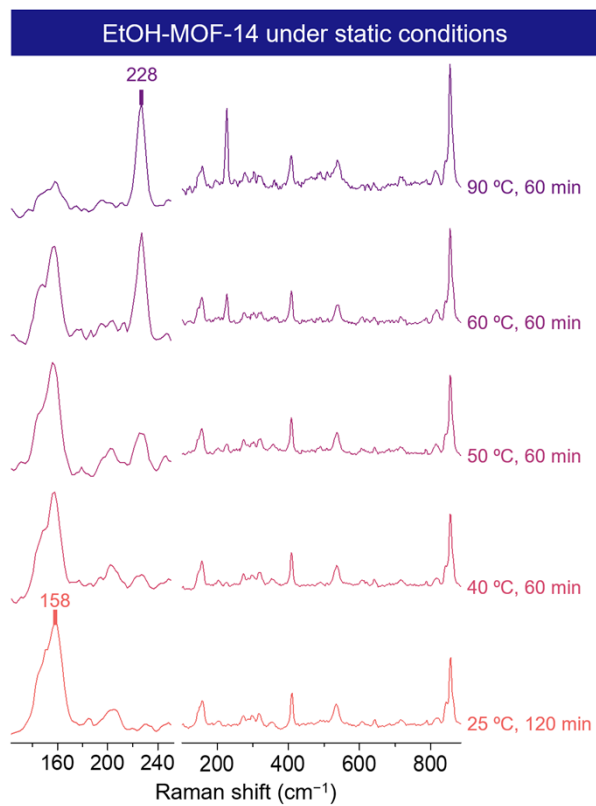


Fig. S24 Narrow (left) and wide (right) views of In situ Raman spectra of EtOH-MOF-14 sample activated under static conditions at various temperatures as indicated.

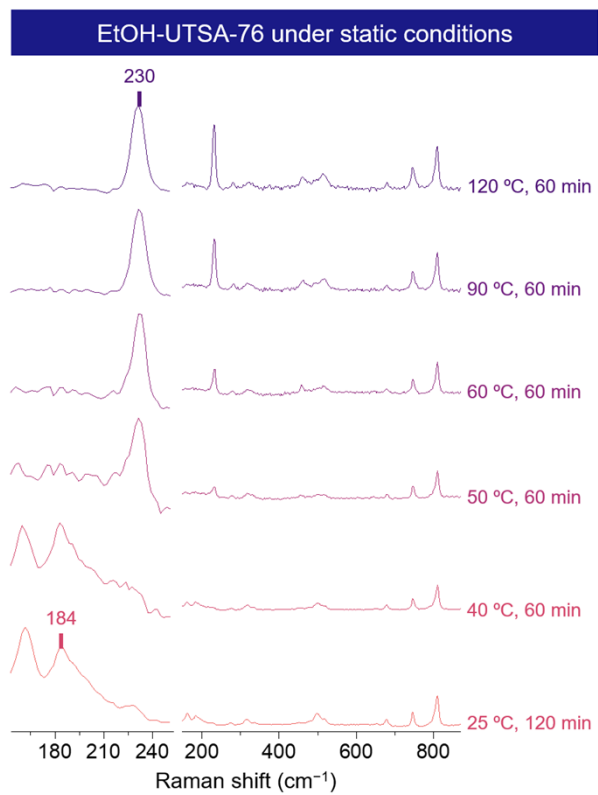


Fig. S25 Narrow (left) and wide (right) views of In situ Raman spectra of EtOH-UTSA-76 sample activated under static conditions at various temperatures as indicated.

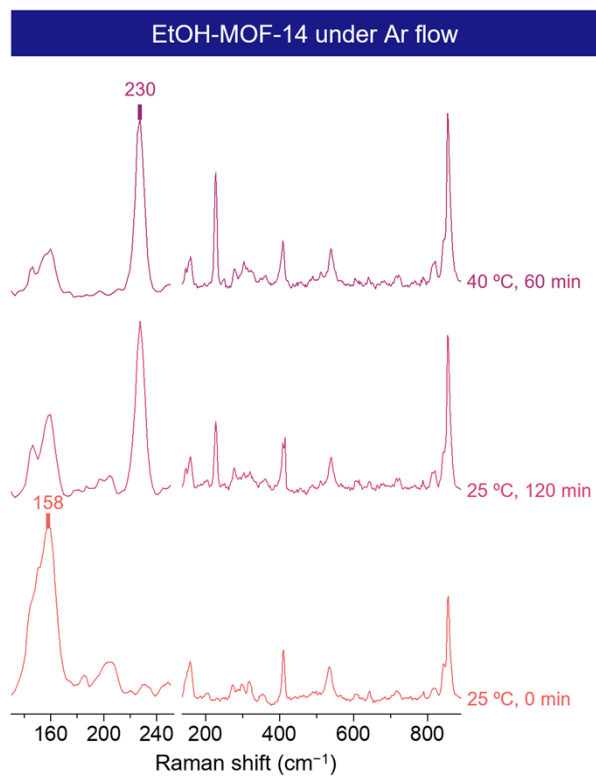


Fig. S26 Narrow (left) and wide (right) views of In situ Raman spectra of EtOH-MOF-14 sample activated under an Ar flow condition ($50 \text{ mL}\cdot\text{min}^{-1}$) at various temperatures as indicated.

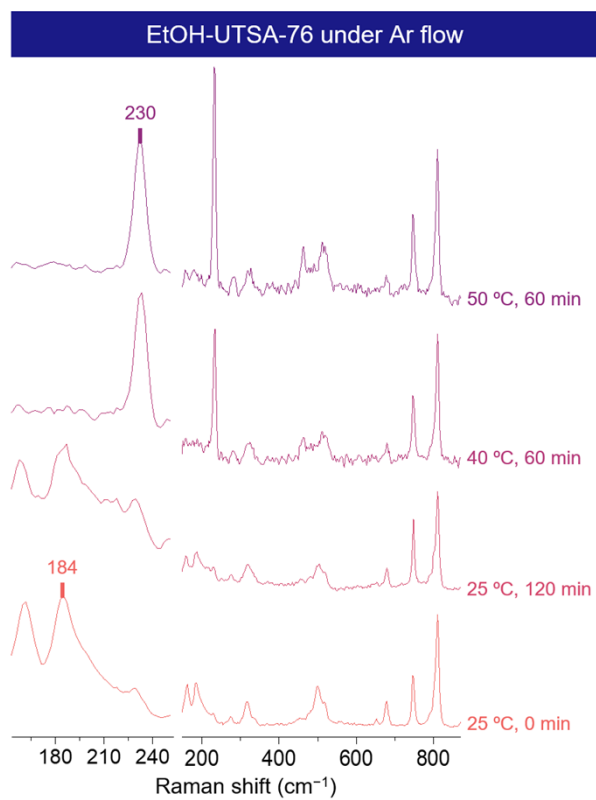


Fig. S27 Narrow (left) and wide (right) views of In situ Raman spectra of EtOH-UTSA-76 sample activated under an Ar flow condition ($50 \text{ mL}\cdot\text{min}^{-1}$) at various temperatures as indicated.

References

1. D. B. Williams and M. Lawton, *J. Org. Chem.*, 2010, **75**, 8351-8354.
2. D. Song, J. Bae, H. Ji, M. B. Kim, Y. S. Bae, K. S. Park, D. Moon and N. C. Jeong, *J. Am. Chem. Soc.*, 2019, **141**, 7853-7864.
3. B. Civalleri, C. M. Zicovich-Wilson, L. Valenzano and P. Ugliengo, *CrystEngComm*, 2008, **10**, 405-410.
4. M. F. Peintinger, D. V. Oliveira and T. Bredow, *J. Comput. Chem.*, 2013, **34**, 451-459.
5. R. Dovesi, R. Orlando, A. Erba, C. M. Zicovich-Wilson, B. Civalleri, S. Casassa, L. Maschio, M. Ferrabone, M. De La Pierre, P. D'Arco, Y. Noël, M. Causà, M. Rérat and B. Kirtman, *Int. J. Quantum Chem.*, 2014, **114**, 1287-1317.
6. R. F. W. Bader, *Atoms in molecules : a quantum theory*, Oxford : Clarendon press, 1990.
7. A. Otero-de-la-Roza, E. R. Johnson and J. Contreras-García, *Phys. Chem. Chem. Phys.*, 2012, **14**, 12165-12172.
8. R. Hernández-Esparza, S.-M. Mejía-Chica, A. D. Zapata-Escobar, A. Guevara-García, A. Martínez-Melchor, J.-M. Hernández-Pérez, R. Vargas and J. Garza, *J. Comput. Chem.*, 2014, **35**, 2272-2278.
9. R. Hernández-Esparza, Á. Vázquez-Mayagoitia, L.-A. Soriano-Agueda, R. Vargas and J. Garza, *Int. J. Quantum Chem.*, 2019, **119**, e25671.
10. H. Babaei, M. E. DeCoster, M. Jeong, Z. M. Hassan, T. Islamoglu, H. Baumgart, A. J. H. McGaughey, E. Redel, O. K. Farha, P. E. Hopkins, J. A. Malen and C. E. Wilmer, *Nat. Commun.*, 2020, **11**, 4010.
11. F. S. Gentile, M. Pannico, M. Causà, G. Mensitieri, G. Di Palma, G. Scherillo and P. Musto, *J. Mater. Chem. A*, 2020, **8**, 10796-10812.
12. M. R. Ryder, B. Van de Voorde, B. Civalleri, T. D. Bennett, S. Mukhopadhyay, G. Cinque, F. Fernandez-Alonso, D. De Vos, S. Rudić and J.-C. Tan, *Phys. Rev. Lett.*, 2017, **118**, 255502.
13. J. Bae, S. H. Park, D. Moon and N. C. Jeong, *Commun. Chem.*, 2022, **5**, 51.
14. S. Van der Perre, T. Van Assche, B. Bozbiyik, J. Lannoeye, D. E. De Vos, G. V. Baron and J. F. M. Denayer, *Langmuir*, 2014, **30**, 8416-8424.
15. R. D. Tosso, O. Parravicini, M. N. C. Zarycz, E. Angelina, M. Vettorazzi, N. Peruchena, S. Andujar and R. D. Enriz, *J. Comput. Chem.*, 2020, **41**, 1898-1911.
16. A. Dhakshinamoorthy, M. Alvaro and H. Garcia, *Catal. Commun.*, 2017, **97**, 74-78.